Surrogate Model on the Extension Operation Range of an Isolated Centrifugal Fan

Z. Li[1], P. Luo [2], M. Zhu [1†], Y. Liu[1] and Z. Chen[1]

[1] School of Aeronautical Engineering, Taizhou University, Jiaojiang, Zhejiang, 318000, China
[2] Zhejiang Yilida Ventilator Co., Ltd., Taizhou, Zhejiang, 318056, China

†*Corresponding Author Email: zhumeijun@tzc.edu.cn*

ABSTRACT

Isolated centrifugal fans are widely utilized in air conditioning system and their performance is closely related to the energy consumption of the system. The purpose of this work is to enlarge the fan operation range without reducing peak efficiency. An improved class and shape function method coupled the Kriging model is proposed to design fan airfoils and to optimize the efficiency and static pressure of the fan. Numerical simulation and experimental study show that both pressure coefficients in large and small flow rate are improved by this optimized fan, and the peak efficiency remains to be unchanged almost under design condition. Optimized pressure coefficient increased by 2.17% in design condition. Furthermore, operation range of the isolated centrifugal fan is enlarged via optimization design scheme and surrogate model. A better understanding of the physical mechanisms involved isolated centrifugal fan is further investigated.

1. INTRODUCTION

Utilization of isolated centrifugal fans in the Heating Ventilation Air Conditioning (HVAC) is employed to drive airflow through ducts (Wolfram & Carolus, 2010). It is generally believed that a higher the maximum efficiency of the fan leads to the improved overall performances. However, it is more crucial for a fan to require a wide operating range rather than only high-efficiency flow points. The objective of this study is to enhance the operational scope of the fan.

Computational fluid dynamics (CFD) is widely employed for the analysis of flow field and optimization of centrifugal fan performance. Immonen (2016) proposed a solution for two engineering design problems that related to the optimal placement of fans in a car park. It is adopted to simulate the airflow and temperature distribution within trains (Jia et al., 2016) as well as pressure with flow rate distribution in central exhaust shaft (Zeng et al., 2022). The results obtained from CFD model exhibited excellent agreement with the experimental data. Wu et al. (Wu et al., 2016) used commercial software to carry out a series of optimization studies on centrifugal fans, including vaneless diffuser and blade optimization based on a semi-empirical model of blade velocity distribution. An intriguing discovery was founded that the dominant patterns of jet-wake flow were attributed to the blockage

of vortex and blade channel, resulting in high velocities on the pressure side of the blade (Li et al. 2020b). The low velocities on the suction side of adjacent blade channel incur shear flow led to a secondary flow and disturbance in the adjacent channel (Johnson & Moore, 1980; Ubaldi et al., 1993). Gap turbulence moving along with the fan shroud can impact the fan blades and contribute to the uneven and unsteady surface pressure distributions among the blades (Ottersten et al., 2021). Regions of higher turbulence kinetic energy between the shroud and blade leading edge are observed on the blade pressure side due to recirculation regions caused by flow passing through the gap (Wolfram & Carolus, 2010). This observation may account for the lower efficiency under off-rated conditions.

The traditional strategies are primarily generated by Bezier curve (Kim et al., 2014), B-spline curve (Mahmood et al., 2016) and NURBS curve (Chen et al., 2006). However, the low-order spline curves fail to accurately describe blades due to the high curvature. Class and Shape functions (CST) can offer a superior approach to achieving a high-precision shape design with fewer design variables, which have been utilized in the field of aerospace engineering, airfoil optimization (Lane & Marshall, 2009), compressor rotor (Tang et al. 2017), and aircraft designs (Liu et al., 2016). The orthogonal

NOMENCLATURE			
C	absolute velocity	$R(x)$	correlation function
$C(x)$	class function	$S(x)$	shape function
c_u	circumferential projection of the absolute velocity	s	streamline direction of the flow
c_m	meridional velocity	$u\ v\ w$	velocity component
D_1	impeller inner diameter	u_2	circumferential speed on blade outlet
D_2	impeller outer diameter	u_z	axial velocity
E	total power	W	relative velocity
H	width of the impeller	w_1	relative velocity on blade inlet
I	incidence angle	Z	rotation axis
K_i	number of combinations components in type function	β_1	inlet angle of the blade
N	order of the Bernstein polynomial	β_2	outlet angle of the blade
n	streamline direction of normal direction	η	static pressure efficiency
n_v	number of fan design variables	μ	molecular viscosity coefficient
P_{st}	static pressure	μ_e	effective viscosity coefficient
P^*	translation pressure	μ_t	turbulent eddy viscosity coefficient
$P_{\varepsilon k},$ $P_{\varepsilon b}$	energy term generated by buoyancy	ρ	air density
P_k	energy term generated by viscous force	τ	pressure coefficient
Q	Q criterion vortex identification method	Φ	flow rate coefficient
Q_m	mass flow rate		

method is also used to improve the number of blades, manufacturing parameters of fan blades, and aerodynamic performance of fans (Li et al., 2020a; Ni et al., 2020). Kim proposed the fourth-order Bezier curve method involved in radial basis neural network and response surface method to optimize the acoustic and aerodynamic design of single-channel axial fan (Kim et al., 2014), and single-channel forward multi-blade centrifugal fans (Heo et al., 2016), respectively. Kim (Kim et al., 2018) adopted a response surface method to optimize the design of impeller and diffuser for mixed-flow pump. Zhou et al. (2021) utilized the Hicks-Henne function to fit the airfoil, as well as incorporated into Kriging model and NSGA method to optimize the efficiency of a centrifugal fan. Compared with other surrogate models, Kriging model is more suitable for low-order nonlinear problems in high-dimensional design space (Li & Zheng, 2017).

The performance of an isolated centrifugal fan was improved by employing a rotating vaneless diffuser (Wu et al., 2017). A method of optimization design for the blade profile of an isolated centrifugal fan by controlling velocity distribution was presented (Wu et al., 2016). The aforementioned studies primarily focus on the single flow rate, demonstrating maximum efficiency point of fan aerodynamic performance. However, this approach is not capacity for meeting the demands of complex operation conditions for fans due to significant influence of multi-point flow rates under different operating conditions. Therefore, it is of great importance to expand the operational range of fans with maximum efficiency via CST method and multi-objective optimization design approach based on Kriging model. The work is validated by experimental data to thereby contribute to enhancing better understanding of physical mechanisms regarding fan operation. It is also doable for optimizing the aerodynamic performance at various flow rates (off-design conditions) for other isolated centrifugal fans within their respective operational ranges.

2. EXPERIMENTS OVERVIEW AND NUMERICAL METHODOLOGY

2.1 Geometry

The isolated centrifugal fan is illustrated in Fig. 1. Three cut planes (planes 1-3) across the fan are specified to observe the flow field in the subsequent analysis. The planes are shown in Fig. 1. Pressure coefficient τ and flow coefficient Φ are defined by:

$$\tau = \frac{2P_{st}}{\rho u_2^{\ 2}} \tag{1}$$
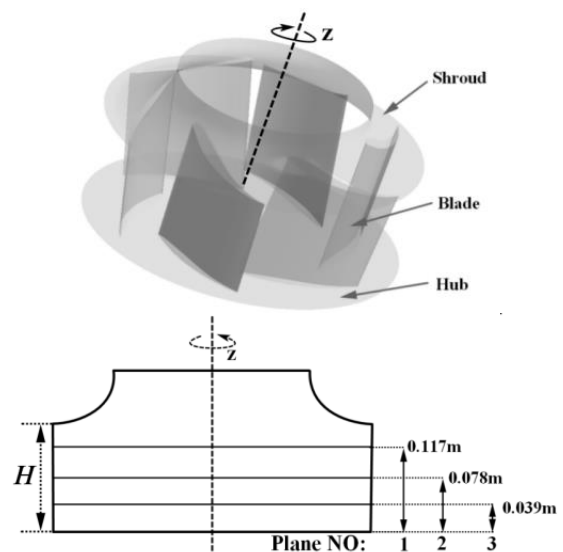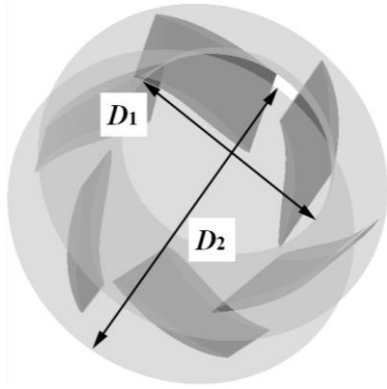
$$\phi = \frac{4Q_m}{\pi D_2^{\ 2} u_2} \tag{2}$$

Fig. 1 Fan geometric configuration

Table 1 Main geometry parameters of the impeller

Parameter	Value
Inner diameter of the impeller (D_1) (mm)	266
Outer diameter of the impeller (D_2) (mm)	460
Outlet angle of the blade (β_2) (°)	28
Number of blades	6
Width of the impeller (H) (mm)	160
Rotation speed (r/min)	700

Fig. 3 Picture of the experimental setup

Fig. 2 Main geometry parameters

where Q_m, P_{st}, D_2, u, and ρ are defined as the flow rate, static pressure, impeller outer diameter, circumferential speed, and air density, respectively.

The main geometry parameters of the impeller are illustrated in Table 1. The inner diameter of the impeller (D_1) and outer diameter of the impeller (D_2) are illustrated in Fig. 2.

2.2 Experimental Facility

The fan installation adopts the method of connecting the pipe inlet and free outlet. The entrance air is taken from a large wind chamber through an inlet nozzle and discharged into a room at standard atmospheric pressure (Fig. 3). The operating flow rate points are controlled by nozzles and an auxiliary fan (Fig. 4). The device description is as follows: 1 electric motor, 2 torque meter, 3 shaft coupling, 4 tested fan, 5inlet duct, 6 fairing, 7 nozzles, 8 auxiliary fan, 9 pressure sensor, 10 data acquisition. The flow rate is measured using Bernoulli equation with the pressure difference across the nozzles.
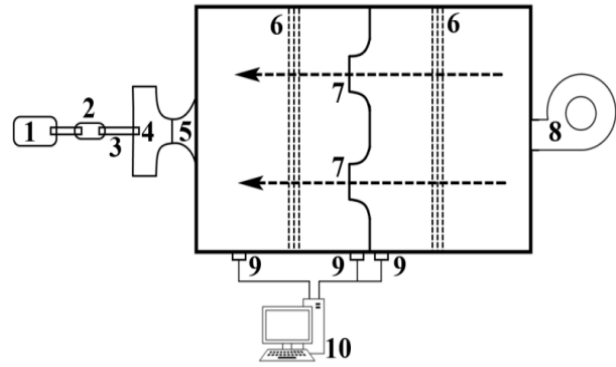
The flow inside the equipment should exhibit a steady with no eddies before measurement. The pressure measurement value is obtained as an average of the pressure values recorded at four pressure monitoring holes, which are uniformly set on the circumferential section of the air chamber at a certain distance across the nozzles. The flow rate Q_m can be determined by calculating the pressure difference ΔP measured across the nozzles.

$$Q_m = f(B)\frac{\pi}{4}\sqrt{2\rho\Delta P}$$

(3)

where B is the parameter of pipe in the fan performance test installation, which are mainly determined by the size

Fig. 4 Test setup and data acquisition system

of wind box, the length of pipes, the size and quantity of nozzles.

The static pressure is measured by four pressure measuring holes located on the cylinder wall, and the average value of the four pressure measuring holes is the static pressure value at the exit of the isolated centrifugal fan. The difference between the inlet and outlet static pressure represents the static pressure of the isolated centrifugal fan. The static pressure efficiency η of the isolated centrifugal fan can be expressed as follows:

$$\eta = \frac{E_e}{E} = \frac{P_s Q_m}{1000E}$$

(4)

where E_e is effective fan power and E is total power calculated by torque meter. The rotating speed and torque of impeller are used to describe the simulation power of the fan. The simulated and experimental results are compared with the mesh-independence verification. The materials for experimental error analysis and laboratory certification have been incorporated to substantiate the reliability of the experimental data. Additionally, we provide comprehensive information on the pressure measuring devices utilized in the experiment, including pressure transmitter (model FCO332-2W of Furness company, instrument numbers 1707230-1707243) and compensatory micropressure meter (model YJB-2500 of Shanghai Yiou company, instrument label 190609). The pressure transmitter automatically collects data, while manual readings are obtained using a compensatory micropressure meter. Both sets of results are compared to ensure the reliability of the experiment.
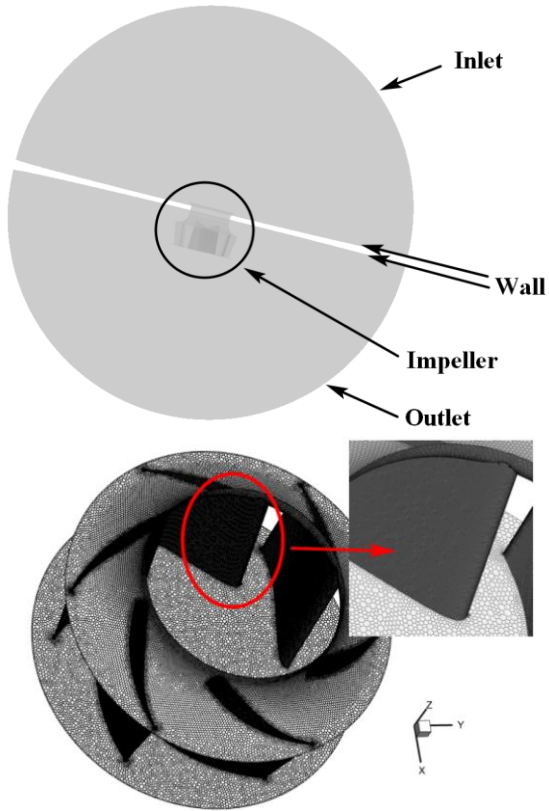
Fig. 5 The computational domains and mesh generation of impeller

Fig. 6 Static pressure with grid number

Tab. 2 Grid-independence verification

Mesh Scheme	No.1	No.2	**No.3**	No.4	No.5
P_s (Pa)	58.8	59.5	**59.6**	59.2	60.2
Mesh (million)	3.05	6.22	**7.45**	11.52	17.21

2.3 Computational Fluid Dynamics Method

The governing equations consist of the continuous equation, the momentum equation and the energy equation. The numerical simulation follows the mass and energy conservation and the Newton second law. The flow in the whole simulation can be considered as incompressible fluid flow with no heat transfer in the process. Fluent software is used for the steady solution of three-dimensional flow field and the standard k-epsilon turbulence model is adopted.

$$\frac{\partial \rho}{\partial t} + \nabla \cdot (\rho \mathbf{U}) = 0 \tag{5}$$

$$\frac{\partial \mathbf{U}}{\partial t} + \nabla \cdot (\mathbf{U}\mathbf{U}) = -\frac{1}{\rho} \nabla p + \nabla \cdot (\nu \nabla \mathbf{U}) \tag{6}$$

where ρ is the density of fluid, $\mathbf{U}$ is the velocity vector, p is the translation pressure and ν is the viscosity coefficient, respectively. The source term is neglected in this equation as we are studying a fluid object consisting of normal temperature air. In order to close the solution equation, k and ε quantities and their related equations are provided.

$$\frac{\partial(\rho k)}{\partial t} + \frac{\partial}{\partial x_i}(\rho u_i k) = \frac{\partial}{\partial x_i}\left[\left(\mu + \frac{\mu_t}{\sigma_k}\right)\frac{\partial k}{\partial x_i}\right] + P_k - \rho\varepsilon + P_{kb} \tag{7}$$

$$\frac{\partial(\rho \varepsilon)}{\partial t} + \frac{\partial}{\partial x_i}(\rho u_i \varepsilon) = \frac{\partial}{\partial x_i}\left[\left(\mu + \frac{\mu_t}{\sigma_\varepsilon}\right)\frac{\partial \varepsilon}{\partial x_i}\right] + \frac{\varepsilon}{k}(C_{\varepsilon 1}P_k - C_{\varepsilon 2}\rho\varepsilon + C_{\varepsilon 1}P_{\varepsilon b}) \tag{8}$$

The four constant coefficients in the above formula are $C_{\varepsilon 1}$=1.44, $C_{\varepsilon 2}$=1.92, σ_k=1.0, σ_ε=1.3, besides, $P_{\varepsilon k}$ and $P_{\varepsilon b}$ represent the energy term generated by buoyancy, while
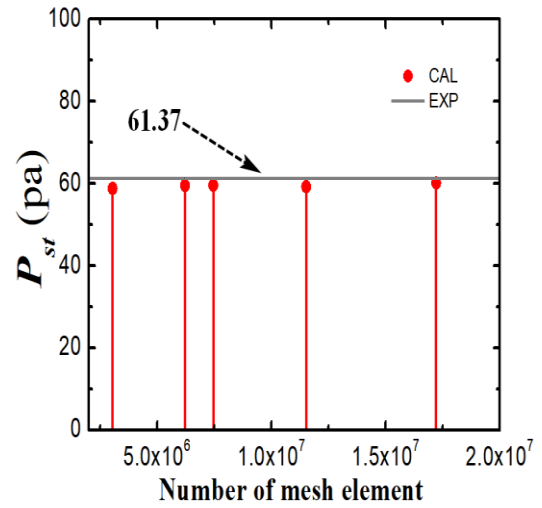
P_k represents the energy term generated by the viscous force. The computational domains and mesh generation of impeller are shown in Fig. 5. The inlet boundary condition was set as the mass flow rate. The outlet boundary condition was set as pressure. The intake airflow was assumed to be fully developed, so the default turbulence quantities were adopted for its turbulence intensity and turbulence viscosity ratio, and were 5% and 10%, respectively. The moving surface and static surface are set as a pair of interfaces to transmit the data between the dynamic and static domains. The whole impeller is set as rotational wall, and all of walls are set as non-slip boundary condition.

The grid-independence test was exclusively conducted for the impeller, while maintaining a consistent cells of 1.22 million for the inlet and outlet extension sections. Consequently, the cells for the impeller are 3.05 million, 6.22 million, 7.45 million, 11.52 million, and 17.21 million are shown in Fig. 6, with an overall rang of the cells of 4.27 million, 7.44 million, 8.67 million, 12.74 million, and 18.43 million. The unstructured grids were used. The number of boundary layers are 8 and the height ratio is 1.1. The $y+$ value at the wall of the rotating region is in the range of 20 to 100. As seen from the Table 2, the error for static pressure is less than 3% by using the 7.45 million scheme. It is selected due to economic CPU time.

The error analysis of experimental results are shown in Fig. 7. The predictions of original fan model are compared with the experimental results. As shown in Fig. 8, the calculations results (CAL) of static pressure (P) and efficiency (E) are well agreed with experimental results (EXP). The rotating speed (700 rmp) and torque of impeller are used to describe the simulation power of the fan.
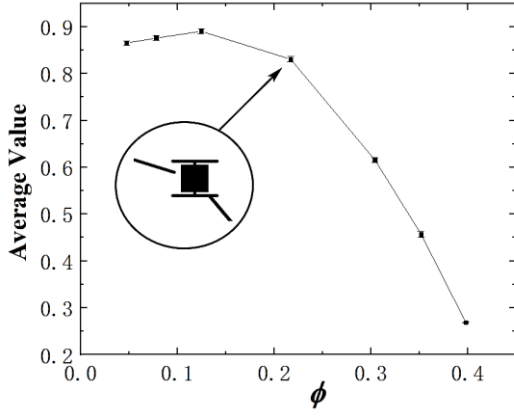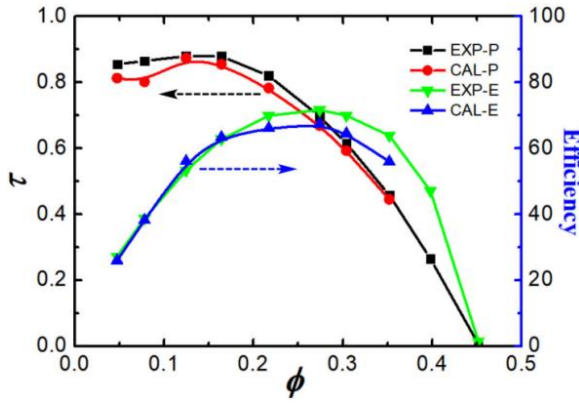
Fig. 7 Error analysis

Fig. 8 Validation of characteristic curves by experimental results

3. PARAMETRIC DESIGN OF BLADE

3.1 Transformation of Coordination

The coordinate system of the impeller differs from the coordinate system used for blade shape parametric design. The coordinate transformation method is utilized to perform the airfoil transformation. It is assumed that the origin of $X' O' Y'$ in XOY is (a,b), and the coordinate axes $O' X'$ and $O' Y'$ are rotated by θ anticlockwise with respect to coordinate axes OX and OY. Consequently, discrete points (x, y) of the blade in coordinate $X' O' Y'$ (x',y') are denoted in XOY:

$$\begin{cases} x = x'\cos\theta - y'\sin\theta + a \\ y = y'\cos\theta + x'\sin\theta + b \end{cases} \tag{9}$$

3. 2 Transformation of coordination

The CST parameterization method was initially proposed by Kulfan B (Kulfan, 2008), which utilizes a category-shape function to describe the geometric shape parameterization characterized by higher precision. It can be defined as follows:

$$\zeta(\psi) = C_{N_2}^{N_1}(\psi) S(\psi) + \psi \Delta \bar{\zeta}_{TE} \tag{10}$$
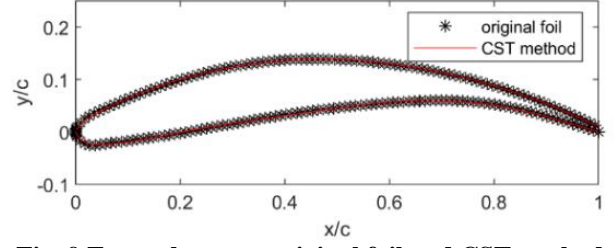

Fig. 9 Errors between original foil and CST method foil

where $\psi = x/c$, and $\Delta\bar{\zeta}_{TE}$ is the trailing edge thickness of the blade representing percentage of chord length, $\Delta\bar{\zeta}_{TE} = \Delta\zeta_{TE}/c$, $\Delta\zeta_{TE}$ is the thickness of the trailing edge.

$$C_{N_2}^{N_1}(\psi) = (\psi)^{N_1}(1-\psi)^{N_2} \tag{11}$$

$$S(x) = \frac{\zeta(x) - \psi\Delta\bar{\zeta}_{TE}}{\sqrt{\psi}(1-\psi)} = \sum_{i=0}^{n}[A_i\psi_i] \tag{12}$$

Where $C_{N_2}^{N_1}(\psi)$ is a class function, $S(\psi)$ is shape-function, N_1=0.5 and N_2=1.0 define the basic geometry. The least square method can be employed to fit the A_i base on the initial blade coordinate points. $S(\psi)$ is the main shape of the blade controlling from the leading to the trailing edge. The Bernstein Polynomial is expressed as follows:

$$BP_{i,n}(\psi) = K_i\psi^i(1-\psi)^{n-i} \tag{13}$$

$$K_i \equiv \binom{N}{i} = \frac{N!}{i!(N-i)!} \tag{14}$$

where K_i is the number of combination components in type function, N is the order of the Bernstein polynomial. Type function for the blades can be defined as follows:

$$S(x) = \sum_{i=0}^{n} A_i BP_{i,n}(\psi) \tag{15}$$

The upper and lower surfaces of blade are fitted by third-order and fourth-order Bernstein polynomials, respectively. The distribution of 100 points on them, as depicted in Fig. 9, exhibits relative errors of less than 1% for each individual point.

3.3 Kriging Model

The Kriging model is a regression algorithm utilized for modeling and predicting random processes by leveraging covariance functions. In the Kriging model, the real unknown function relationship between the observed value Y and the design variable is the covariance matrix of $Z(x)$.

Where **R** is the correlation function, the maximum likelihood function of the data observation and the forecast model are taken by the natural logarithm.

$$y(x) = f(x) + Z(x) \tag{16}$$

$$\text{Cov}\left[Z\left(x^{(i)}\right), Z\left(x^{(j)}\right)\right] = \sigma^2 \mathbf{R}\left[\mathbf{R}\left(\mathbf{x}^{(i)}, \mathbf{x}^{(j)}\right)\right] \tag{17}$$
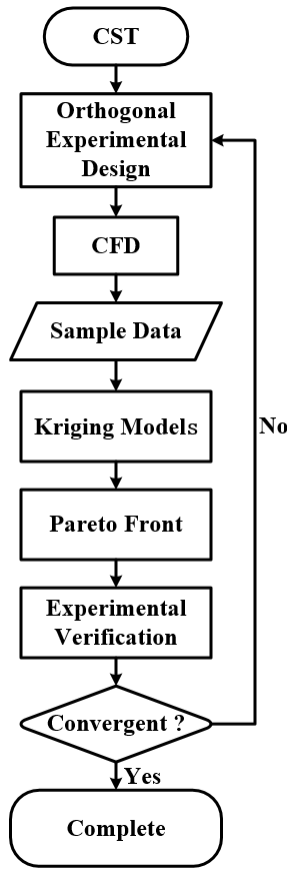
Fig. 10 Optimization design scheme of fans

Fig. 11 Blades and Tested fans

Fig. 12 The pressure experimental results of the original model(O) and the optimized model (I)

$$R\left(x^{(i)}, x^{(j)}\right) = \exp\left[-\sum_{k=1}^{n_v} \theta_k \left|x_k^{(i)} - x_k^{(j)}\right|^2\right] \tag{18}$$

The nonlinear problem of the equation above can be solved in order to obtain the blade geometry of the fan (Santner et al. 2003).

$$r^T(x) = \left[R(x, x^1), R(x, x^2), \cdots, R(x, x^{n_s})\right]^T$$

$$-\frac{\left[n_s \ln\left(\hat{\sigma}^2\right) + \ln|\mathbf{R}|\right]}{2} \tag{19}$$

It is indicated that efficiency and static pressure of the fan is closely related to blade geometry by Kriging model. Different blade parameters of fan performance with high fidelity is demonstrated by numerical method and Pareto front was obtained. Therefore, different optimization targets can be achieved by the optimized blade airfoil parameters. The optimization design scheme is shown in Fig. 10.

4. RESULT AND DISCUSSION

The chord length and blade height of the blade are identical, as well as the shroud and hub dimensions. The differences of the original and optimized blades and the two impellers are shown in Fig. 11. The impellers were fabricated with resin and adjusted with dynamic balancing techniques. Both impellers are capable of operating at 1000rpm. The fan speed in this paper is set at 700 rpm for the purpose of ensuring safety.
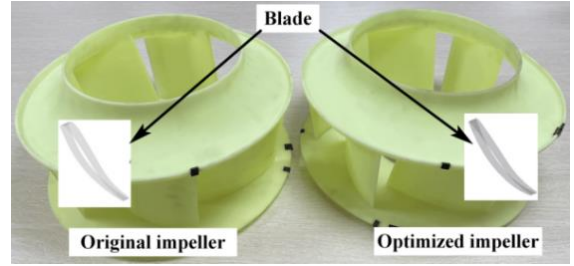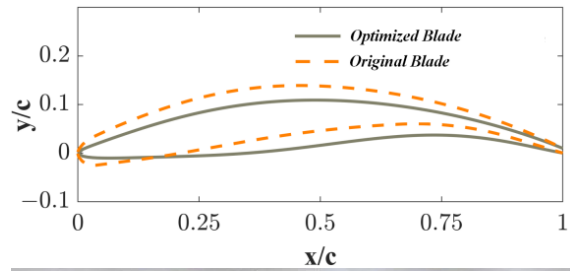
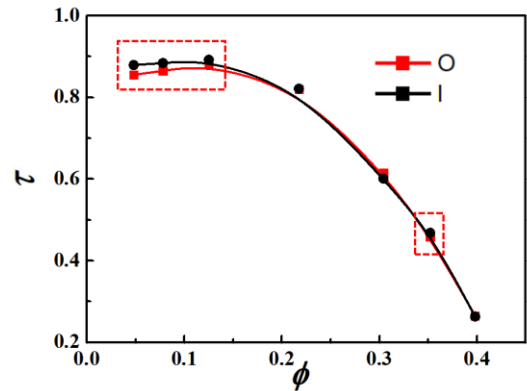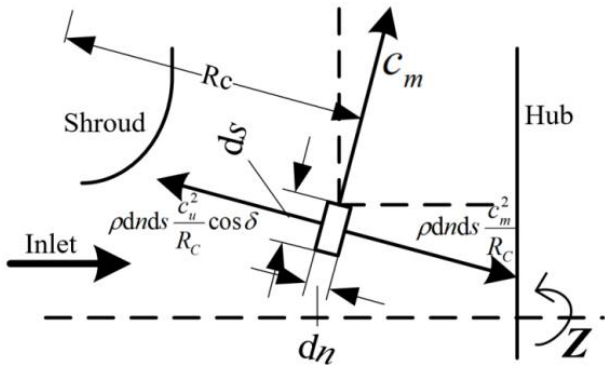The experimental results of the two impellers are exhibited in Table 3. It can be observed that both pressure coefficients at high and low flow rate are improved with optimized impeller, while the maximum efficiency point remains almost unchanged. As shown in Fig. 12 and Tab. 3, the pressure coefficient of the optimized model is increased by 2.17% at φ=0.352, whereas it increases by 1.45% at φ=0.125. The range between coefficient of 0.125 and 0.352 exhibits a static pressure efficiency exceeding 50%, which can be considered as the operational range for the fan. It proves that the operation range of the isolated centrifugal fan can be improved by optimization design scheme depended on surrogate model.

The following is the result and discussion for flow coefficient at 0.352, velocity changes from axial to radial direction after the airflow passing through the impeller from inlet to outlet. The force of fluid element on the meridian plane is illustrated in Fig. 13. Where s is the streamline direction of the flow and n is normal direction, R_c is radius of blade curvature, c_u is the circumferential projection of the absolute velocity, c_m is the meridional velocity, ρ is air density, Z is the rotation axis. The normal force balance is as follows:

$$\rho \mathrm{d}n\mathrm{d}s \frac{c_u^2}{R_C}\cos\delta - \rho \mathrm{d}n\mathrm{d}s \frac{c_m^2}{R_C} - \frac{\mathrm{d}p}{\mathrm{d}n}\mathrm{d}n\mathrm{d}s = 0 \tag{20}$$

Table 3 The experimental results of the original model and the optimized model

Flow coefficient	Pressure coefficient of original model	Pressure coefficient of optimized model	Increase of pressure coefficient (%)	Efficiency of original model (%)	Efficiency of optimized model (%)	Increase of efficiency (%)
0.398	0.265	0.263	-0.89	47.11	46.22	-1.89
0.352	0.458	0.468	2.17	63.88	62.91	-1.52
0.304	0.615	0.601	-2.22	69.95	69.88	-0.09
0.2174	0.820	0.821	0.10	69.91	69.82	-0.13
0.125	0.880	0.892	1.45	53.31	53.18	-0.24
0.078	0.865	0.884	2.22	38.74	39.43	1.77
0.048	0.855	0.879	2.85	27.16	28.03	3.21

Fig. 13 The force of fluid element on the meridian plane

Fig. 14 Streamlines and relative velocity contours (cut) on meridian plane (a) Original impeller (b) Optimized impeller
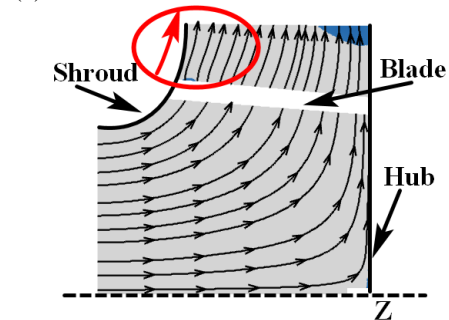
The first term represents the inertial centrifugal force, while the second term denotes the normal projection of the inertial force caused by implicated acceleration. The last term is pressure difference in the normal direction. The gap turbulence evolves with shroud. It is subsequently carried downstream to impinge on blades (Ottersten et al., 2021). Moreover, if blade design is unreasonable, this turbulence can be further intensified.

The streamlines and relatively positive velocity contours on the meridian plane are shown in Fig.14. The circumferential velocity near the shroud is larger than the radial velocity for gap turbulence. Moreover, the differences of pressure near the shroud is greater than that of in the center of the impeller, leading to a flow crashing on the shroud. The most significant impingement is observed on the top side of the blade leading edges in the vicinity of shroud.

The streamlines of the two impellers exhibit a noticeable difference in the flow behavior at the shroud. Specifically, the streamline at the same position on the improved impeller appears to be smoother compared to that on the original impeller. This can be attributed to uneven gap turbulence occurring along the leading edge of blades (Ottersten et al., 2021). Meanwhile, the relatively positive velocity means the velocity direction is coming from hub to shroud (see Fig 14(a)), and this region is closely to shroud for original impeller. The blue areas represent air flow velocities below 0.9m/s. As mentioned above, the difference of pressure caused by gap turbulence lead to friction and energy loss in airflow, which is heavily intensified by the leading edge of blades with lager

thickness. However, in contrast to the original impeller, the distributions of relative velocity near shroud of improved impeller is better.

The static pressure contours of the blade leading edge on both suction and pressure surface are shown in Fig. 15. A similar region of lower pressure is observed on the leading edge of suction surface near shroud in both two impellers, as predicted by CFD simulation. Additionally, non-uniform pressure distribution near the shroud of the original model blade is also found. In this region, contours are being distorted along leading edge of blade. However, for the improved impeller, these contours exhibit a more uniform distribution and do not indicate significantly lower pressures. Moreover, regions inside the fan can easily lead to energy loss, while those on the fan will increase the friction effect and energy loss in the gas transport process. Therefore, lower pressure region on pressure surface of blade is eliminated by the optimized impeller, and its distribution is more uniform along radial direction between shroud and leading edge.
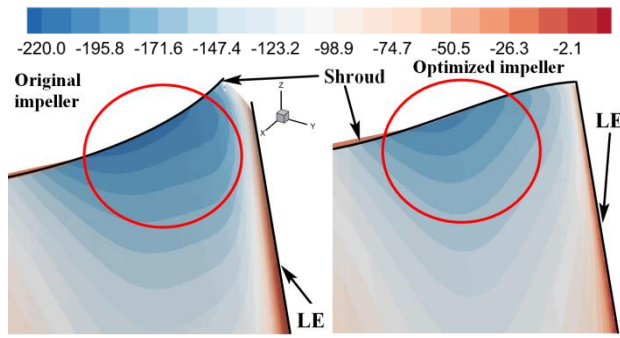
(a)
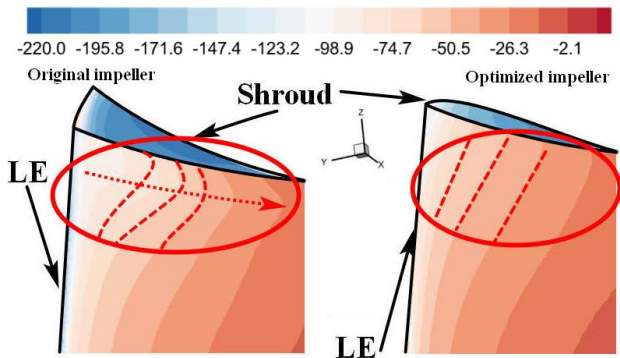
(b)

**Fig. 15 Static pressure contour of blade leading edge
(a) Suction surface (b) Pressure surface**

The schematic diagram of incidence angles I with different flow rates and streamline on the radial plane are shown in Fig. 16. Where c_1 is the absolute velocity, u_1 is circumferential velocity, w_1 is relative velocity, and the subscript 1 means the inlet of blade as follows:

$$I = \beta_1 - \beta_1'$$

(21)

The incidence angle of blade inlet side is defined as the difference between the blade inlet angle, inlet relative velocity and circumferential tangent, which is varying with the flow rate. Under design conditions, airflow enters the blade passage along the tangent direction of the blade inlet, determined by a zero-thickness blade. A larger thickness at the leading edge is typically designed for impeller blade. Consequently, real streamline (dotted curve) will be distort when passing through blade leading edge under lager flow rate with small incidence angle, which are quietly different from the ideal relative velocity direction w_1` (solid curve). The superscript ' indicates conditions exceeding the design flow rate, while the superscript " indicates conditions below the design flow rate. Airflow generates a closed vortex region on pressure surface that closely to the leading edge and shroud, especially for larger flow rate. But it is eliminated with rational direction of blade.

Figure 17 shows the streamlines upstream of the blade inlet around pressure surface at lager flow rate. The blade inlet refers to the leading edge of the airflow passage between the two blades, while the blade leading edge refers to the foremost part of an individual blade. No modifications have been made to either the leading edge
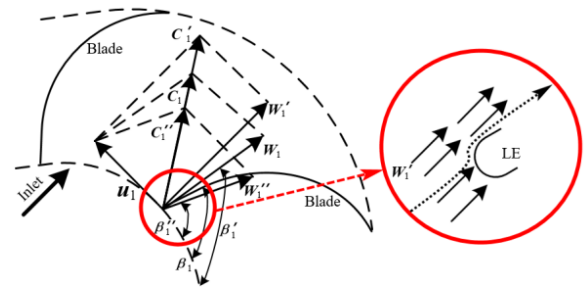
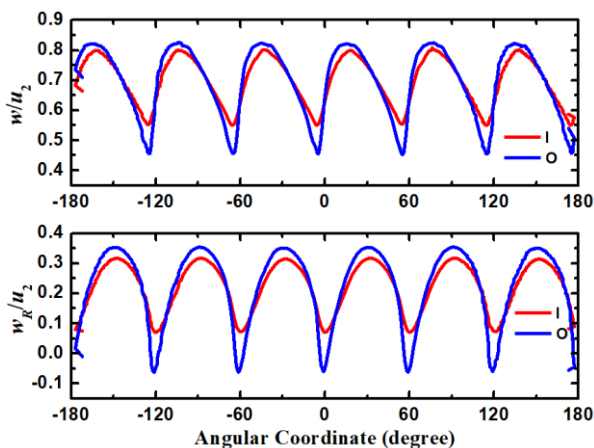**Fig. 16 Schematic diagram of incidence angle**
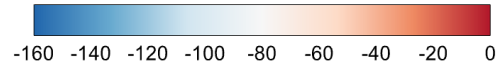
(a)
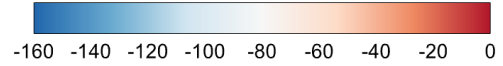
(b)

**Fig. 17 Streamlines of the blade inlet around pressure
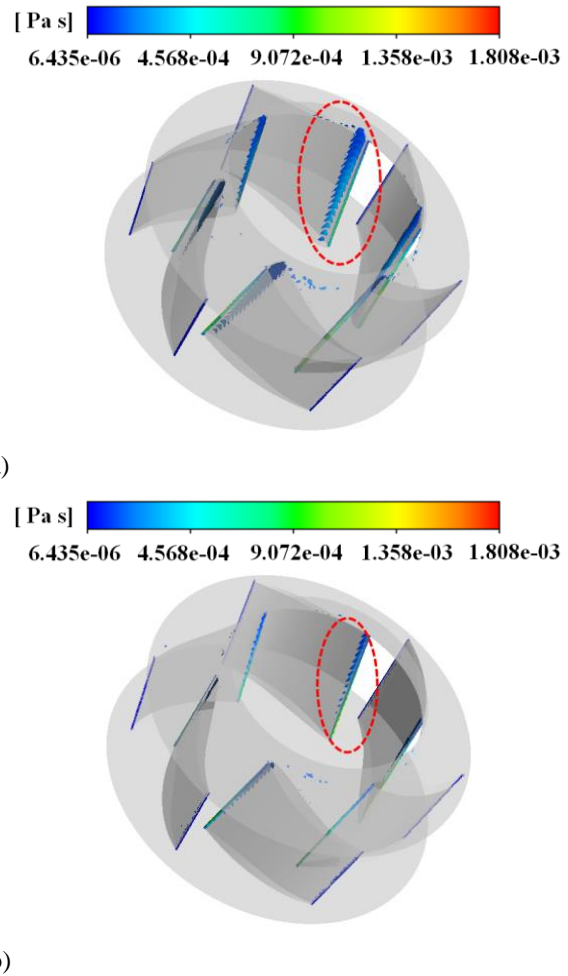surface (a) Original impeller (b) Optimized impeller**

point or end point of the blade airfoil, and its chord length remains unaltered as well. Therefore, there is no change in the angle of attack of the airfoil. The symmetric inflow is not disturbed far from the upstream impeller. However, as the flow enters the blade inlet, flow velocity decreases gradually along the streamlines on pressure surface as incidence angle decrease when flow enters the blade inlet. As shown in Fig 17. (a), the airflow generates a closed vortex on the pressure surface that closely to leading edge and shroud in origin impeller. Backward flow is also found at leading edge. These can be used for explaining that uneven and unsteady surface are favorable for the formation of the adverse pressure gradient distribution among the blades near shroud. The backward flow region in optimized impeller and the higher pressure region at the stagnation point of the leading edge are neglect able. With the increase of mass flow, the impact of the airflow in the stage is being intensified. Furthermore, vortex region is being cut down for optimized impeller with the thinner blade leading edge (see Fig. 17 (b)).

The relative velocity w and radial velocity w_R along the blade inlet near leading edge on plane 2 are shown in Fig. 18, where u_2 is the circumferential velocity of blade outlet. The crest represents the position at the center of the two blades, while trough represents the location near the leading edge of the blades. Consequently, six crests and troughs represent each of the six blades. Although maximum inlet velocity of both impellers are approximately similar and their distributions and maximum inlet velocity are different, which result in friction and energy loss for air flows and those of optimized impeller (I) are uniform, as well as smaller velocity change. Radial velocity at near blade of original impeller (O) is less than zero (see Fig. 18), in which back flow blocks the inlet flow passage. Those velocity of original model increases leading to the formation of velocity in blade passage and large jet-wake pattern on blade outlet.

Figure 19 demonstrates the distributions of three-dimensional vortex in the impellers, where the Q value (Q criterion vortex identification method) is approximately divided into two parts the leading and trailing edge of blades. Larger magnitudes are commonly found at the blade leading edges that close to the shroud. Locations

(a)

(b)

Fig. 19 Vortex distribution in the impellers (a) Original impeller (b) Optimized impeller

with higher energy are similar to those turbulent regions leading to impingement on the walls. Turbulence intensity refers to the ratio of fluctuation standard deviation to average velocity of turbulence intensity. It increases gradually along the direction from hub to shroud, accounting for the uneven and unsteady surface which the distributions of pressure gradient adverse among the blades. Compared to Q values of original model, those improved models exhibit smaller values. This leads to a decrease in friction and energy loss for optimized impeller designs with thinner blade leading edges.

$$Q = -\frac{1}{2}\left(\left(\frac{\partial u}{\partial x}\right)^2 + \left(\frac{\partial v}{\partial y}\right)^2 + \left(\frac{\partial w}{\partial z}\right)^2\right)$$
$$-\frac{1}{2}\frac{\partial u}{\partial y}\frac{\partial v}{\partial x} - \frac{1}{2}\frac{\partial u}{\partial z}\frac{\partial w}{\partial x} - \frac{1}{2}\frac{\partial v}{\partial z}\frac{\partial w}{\partial y} \tag{23}$$

The axial eddy and the pressure difference distributions on the blade pressure and suction surfaces, as well as the airflow near the impeller outlet, are observed to be smooth in Fig. 20 due to the combined effect of blade rotations. The axial eddy is a result of inertia, causing air flow movement in the direction of impeller rotation. The jet-wake pattern predicted by prediction is primarily caused by the structure of centrifugal fans and cannot be completely eliminated even with alleviations. The circumferential velocity exhausted from the impeller
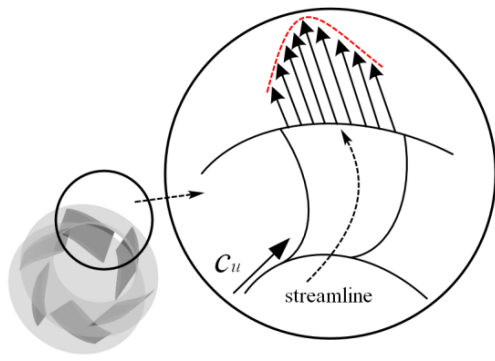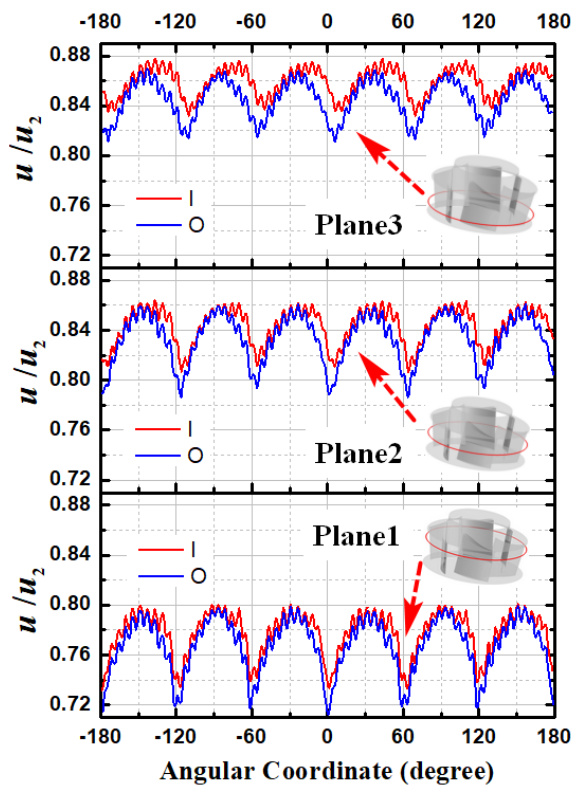

Fig. 18 Relative velocity and radial velocity along blade inlet near leading edge

Fig. 20 Jet-wake patterns

Fig. 21 Relative velocity distribution of impeller

Fig. 22 Static pressure distribution of impeller
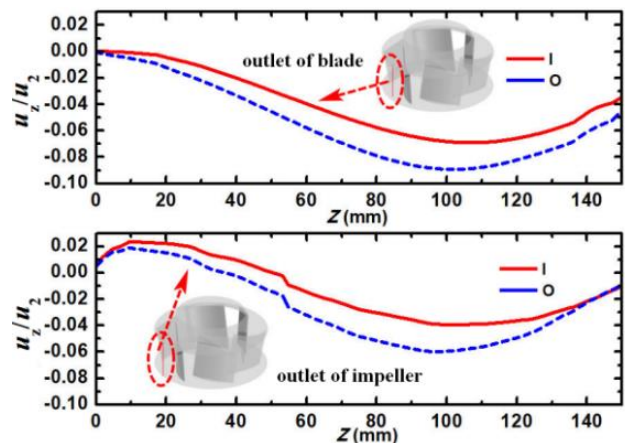
Fig. 23 Axial velocity distribution along shroud to hub on impeller outlet

generates this jet-wake pattern, leading to a strong shear flow resulting in significant energy loss. Airflow is deflected early at regions close to shroud, which are marked by circles. Furthermore, there are variations in outlet velocities due to uneven upstream distribution, and some differences between both impellers can be observed at corresponding positions.

The distributions of relative velocities and static pressure at three cut planes of impeller outlet are used to compare the jet-wake phenomena under the lager flow rate conditions (see Fig. 21 and 22). The optimized impeller demonstrates enhanced uniformity and incurs lower velocity fluctuations. The accumulation and release of fluid energy in impeller passages are the primary reasons for propagation starting from upstream blade inlet. Moreover, the closer to shroud the airflow is, the bigger the velocity difference is. As can be seen from the figures, a larger amplitude of airflow velocity fluctuation is found,
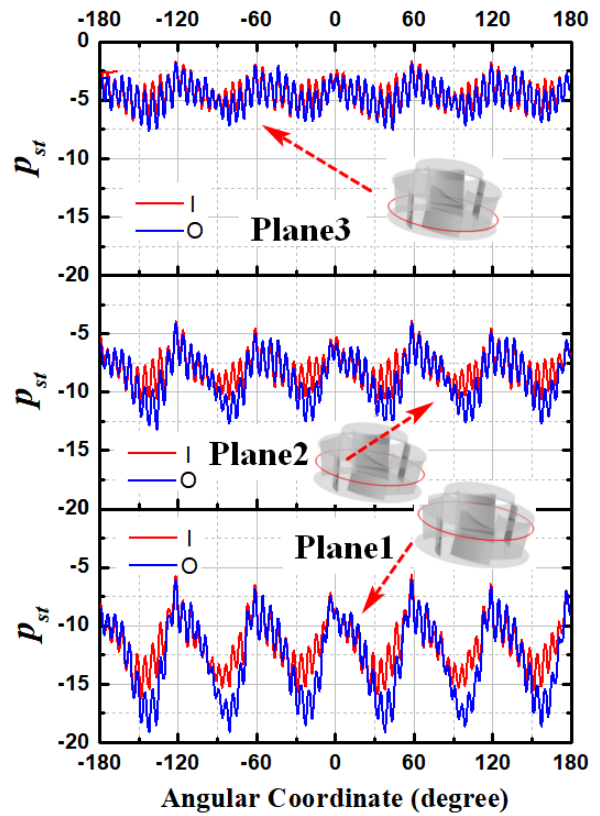
while the relative velocity at outlet demonstrates an overall increasing trend from shroud to hub. Mass flow in the passage near shroud is reduced, and total mass flow through the impeller remains to be unchanged. Energy loss are caused by the velocity and static pressure fluctuation of original impeller even no separation phenomenon by jet-wakes. Flow friction and energy loss among impeller outlets are weakened by optimized blades.

The radial airflow from the impeller should be with an axial velocity (u_z). The distributions of axial velocity along the shroud to hub at the impeller outlet are shown in Fig. 23, where Z=0(mm) is the position of the hub. The direction of negative axial velocity is starting from shroud

to hub. Axial velocity at outlet along shroud to hub of improved impeller is smaller. Maximum axial velocity of the original model is twice that of the improved model, which increases rapidly near shroud due to the impact energy (see Fig. 23). In summary, primary reason of lower static pressure in original model are not matched well between leading edge and upstream near the shroud side. Additionally, design defects for original impeller are inherent. Therefore, the original impeller is replaced by optimized impeller in order to improve the static pressure and efficiency of the fan.

5. CONCLUSION

In this work, the operation range of isolated centrifugal fan was enlarged by optimization design scheme with surrogate model. The CST method and multi-objective optimization are carried out based on the Kriging model for the extension of fan operation without the reduction of peak efficiency. Experimental data, numerical simulation and surrogate model are utilized to testify successfully the optimization accuracy and reliability. The pressure coefficient of optimized model increased by 2.17%, 1.45% at $\varphi = 0.352$ and at $\varphi = 0.125$, respectively., indicating that static pressure efficiency is in the excess of 50% and can be considered as the operational range. However, some limitations of this study should be further improved, such as implementation of chord length, and attack angel optimization airfoil blade.

ACKNOWLEDGEMENTS

CONFLICT OF INTEREST

The authors declare there are no known conflicts of interest associated with this publication and there has been no significant financial support for this work that could have influenced its outcome. We confirm that the paper has been read and approved by all named authors and that there are no other persons who satisfied the criteria for authorship but are not listed.

AUTHORS CONTRIBUTION

Writing — Original Draft Preparation, **Z. Li**; Data Curation, **P. Luo**; Review & Editing, **Y. Liu**; Modifications of Figures, **Z. Chen**; Project Administration, **M. Zhu**. All authors have read and agreed to the published version of the manuscript.

REFERENCES

Chen, B., Gao, X., & Yuan, X. (2006). Aerodynamic 3-dimensional optimal design by NURBS of a certain stage turbine blades. *Journal of Chinese Society of Power Engineering, 26*(2), 201-206. https://doi.org/10.3969/j.issn.1674-

7607.2006.02.008

Heo, M., Kim, J., & Seo, T. (2016). Aerodynamic and aeroacoustic optimization for design of a forward-curved blades centrifugal fan. *Proceedings of the Institution of Mechanical Engineers, Part A: Journal of Power and Energy, 230*(2), 154-174. https://doi.org/10.1177/09576509156246

Immonen, E. (2016). CFD optimization of jet fan ventilation in a car park by fractional factorial designs and response surface methodology. *Building Simulation, 9*(1), 53-61. https://doi.org/10.1007/s12273-015-0249-0

Jia, Q., Xia, C., & Zang, J. (2016). Numerical simulation on the temperature field in an equipment cabin of a high-speed railway train. *Building Simulation, 9*(6), 689-700. https://doi.org/10.1007/s12273-016-0298-z

Johnson, M., & Moore, J. (1980). The development of wake flow in a centrifugal impeller. *Journal Engineering for Power, 102*(2), 382-389. https://doi.org/10.1115/1.3230265

Kim, J., Ovgor, B., & Cha, K. (2014). Optimization of the aerodynamic and aeroacoustic performance of an axial-flow fan. *AIAA Journal, 52*(9), 2032-2044. https://doi.org/10.2514/1.J052754

Kim, S., Lee, K., & Kim, J. (2018). Design of mixed-flow pump for Ns475 based on optimum design database. *International Journal of Fluid Machinery and Systems 11*(2), 123-128. https://doi.org/10.5293/IJFMS.2018.11.2.123

Kulfan, B. (2008). Universal parametric geometry representation method. *Journal of Aircraft, 45*(1), 142-158. https://doi.org/10.2514/1.29958

Lane, K., & Marshall, D. (2009, January). *A surface parameterization method for airfoil optimization and high lift 2D geometries utilizing the CST methodology*. 47th AIAA Aerospace Sciences Meeting, Florida, USA. https://doi.org/10.2514/6.2009-1461

Li, Z., & Zheng, X. (2017). Review of design optimization methods for turbomachinery aerodynamics. *Progress in Aerospace Sciences, 93*, 1-23. https://doi.org/10.1016/j.paerosci.2017.05.003

Li, Z., Dou, H., & Lin, P. (2020a). Design for a squirrel cage fan with double arc blade. *Journal of Applied Fluid Mechanics, 13*(3), 881-891. https://doi.org/10.29252/JAFM.13.03.30551

Li, Z., Luo, P., & Zhu, M. (2023). Effect of motor installation heights on the performance of an isolated centrifugal fan. *Processes, 11*(7), 2116. https://doi.org/10.3390/pr11072116

Li, Z., Ye, X., & Wei, Y. (2020b). Investigation on vortex characteristics of a multi-blade centrifugal fan near volute outlet region. *Processes, 8*(10), 1240. https://doi.org/10.3390/pr8101240

Liu, C., Duan, Y., & Cai, J. (2016). Application of the 3D multi-block CST method to hypersonic aircraft optimization. *Aerospace Science and Technology 50*,

295-303. https://doi.org/10.1016/j.ast.2015.06.019

Mahmood, S., Turner, M., & Siddappaji, K. (2016, June). *Flow characteristics of an optimized axial compressor rotor using smooth design parameters.* Turbo Expo: Power for Land, Sea, and Air. American Society of Mechanical Engineers, Seoul, South Korea. https://doi.org/10.1115/GT2016-57028

Ni, J., Liu, R., & Sun, Y. (2020). Multidisciplinary assessment of blade number and manufacturing parameters for the performance of centrifugal fans. *Proceedings of the Institution of Mechanical Engineers Part A: Journal of Power and Energy, 235*(4), 766-782. https://doi.org/10.1177/0957650920957465

Ottersten, M., Yao, H., & Davidson, L. (2021). Tonal noise of voluteless centrifugal fan enerated by turbulence stemming from upstream inlet gap. *Physics of Fluids 33*, 075110. https://doi.org/10.1063/5.0055242

Santner, J., Williams, J., & Notz, W. (2003). *Design and analysis of computer experiments.* Springer Verlag, Berlin, Germany. https://doi.org/10.1007/978-1-4939-8847-1

Tang, X., Luo, J., & Liu, F. (2017). Aerodynamic shape optimization of a transonic fan by an adjoint-response surface method. *Aerospace Science and Technology 68*, 26-36. https://doi.org/10.1016/j.ast.2017.05.005

Ubaldi, M., Zunino, P., & Cattanei, A. (1993, May). *Relative flow and turbulence measurements downstream of an axial flow rotor.* Proceedings of the Second International Symposium on Engineering Turbulence Modelling and Measurements, Florence, Italy. https://doi.org/10.1016/0894-1777(94)90111-2

Wolfram, D., & Carolus, T. (2010). Experimental and numerical investigation of the unsteady flow field and tone generation in an isolated centrifugal fan impeller. *Journal of Sound & Vibration, 329*(21), 4380-4397. https://doi.org/10.1016/j.jsv.2010.04.034

Wu, L., Dou, H., & Wei, Y. (2016). Optimization of blade profile of a plenum fan. *International Journal of Fluid Machinery & Systems, 9*(1), 95-106. https://doi.org/10.5293/IJFMS.2016.9.1.095

Wu, L., Dou, H., & Wei, Y. (2017). Employing rotating vaneless diffuser to enhance the performance of plenum fan. *International Journal of Fluid Machinery & Systems 10*(1), 9-18. https://doi.org/10.5293/IJFMS.2017.10.1.009

Zeng, L., Tong, L., & Gao, J. (2022). Pressure and flowrate distribution in central exhaust shaft with multiple randomly operating range hoods. *Building Simulation, 15*(1), 149-165. https://doi.org/10.1007/s12273-021-0786-7

Zhou, S., Zhou, H., & Yang, K. (2021). Research on blade design method of multi-blade centrifugal fan for building efficient ventilation based on Hicks-Henne function. *Sustainable Energy Technologies and Assessments 43*, 100971. https://doi.org/10.1016/j.seta.2020.100971